https://doi.org/10.1016/j.mtener.2021.100720

Metal-free Tellurene Cocatalyst with Tunable Bandgap for Enhanced Photocatalytic Hydrogen Production

Bocheng Qiu,[a,b,c] Cong Wang,[b,c] Jingli Wang,[b,c] Ziyuan Lin,[b,c] Ning Zhang,[b,c] Lejuan Cai,[b,c] Xiaoming Tao[d] and Yang Chai[b,c]*

a. Jiangsu Key Laboratory of Pesticide Sciences, Department of Chemistry, College of Sciences, Nanjing Agricultural University, Nanjing 210095, PR China.

b. Department of Applied Physics, The Hong Kong Polytechnic University, Hung Hom, Kowloon, Hong Kong, 999077 P. R. China.

c. The Hong Kong Polytechnic University Shenzhen Research Institute, Shenzhen, 518057 P. R. China.

d. Institute of Textiles & Clothing, The Hong Kong Polytechnic University, Hung Hom, Kowloon, Hong Kong, 999077 P. R. China.

* Corresponding author: Yang Chai. Email address: ychai@polyu.edu.hk

Abstract

The discovery of metal-free elemental cocatalysts has spurred dramatic advances in the field of photocatalysis. Bandgap engineering has always been used as an effective approach to make these cocatalysts form favorable band alignment with photocatalysts. Here, we develop metal-free tellurene (Te) with largely tunable bandgap as a highly efficient cocatalyst and investigate its thickness-dependent catalytic activity. Our experimental and theoretical studies reveal that the increased reduction potential of conduction band (CB) together with the decreased thickness, abundant active sites and high charge mobility of tellurene, as well as the strong electronic coupling effects between tellurene and metal sulfides enable the enhanced photocatalytic hydrogen evolution rate and high quantum efficiency of 11.4% under the light illumination with the wavelength of 420 nm. This work enriches our understanding of the structure-activity correlations for tellurene and opens a path for solar energy harvesting from artificial photosynthesis by robust and cost-effective photocatalysts.

Keywords: Tellurene; tunable bandgap; metal-free cocatalysts; photocatalytic hydrogen evolution.

1. Introduction

Photocatalytic conversion of solar energy to fuels and chemicals is an attractive prospect for the storage of renewable energy, while the relatively low energy conversion efficiency remains the greatest challenge in developing this technology on a large scale.[1-4] In principle, there are three key steps during photocatalytic process: the generation of electron-hole pairs upon solar-light irradiation, their subsequent separation and immigration, and their participation in surface redox reactions.[5, 6] To achieve highly efficient photocatalytic conversion, the most critical factor is to suppress recombination of photogenerated electron-hole pairs. It is highly demanded to accelerate electron transfer kinetics for electron-evolved photocatalytic hydrogen evolution reaction, which is achieved by the introduction of cocatalysts.[7-9] The presence of cocatalyts can promote separation and transfer of electron–hole pairs, and improve catalytic activity for photocatalytic water reduction.[10, 11] To date, most cocatalysts are based on transition metal, especially for noble metal Pt, which suffers from high cost and scarcity.[12-15] In this context, it is highly desirable to develop new metal-free cocatalyst that can rapidly transfer photogenerated electron, which still remains a huge challenge.

Over the past decade, substantial works have uncovered that a good cocatalysts should have these basic features: 1) modulated band gap providing potential to form favorable band alignment with photocatalysts;[16-18] 2) high carrier mobility to

transfer photogenerated charges;[19, 20] 3) large surface area enabling abundant active site involved in the catalytic reaction.[21, 22] 4) strong oxidation resistance when exposed to the air.[23, 24] Based on these principles, two-dimensional (2D) elementary materials including graphene[24, 25] and black phosphorene,[26, 27] have been investigated as metal-free cocatalysts owing to their intriguing properties of high carrier mobility, large surface area, and strong optical absorption. Distinct from their bulk counterparts, 2D materials possess exotic electronic and photonic properties, especially large photoreactive contact and thickness-dependent band gap, providing them great possibilities to form favorable band structure with photocatalysts. However, these 2D materials as cocatalysts do not possess all desirable optoelectronic properties required in photocatalysis. For instance, graphene is semimetallic with zero band gap.[28] Black phosphorene has a layer-dependent band gap from 0.3 to 2.0 eV and high carrier mobility, but it suffers from instability in air and water.[29-31] As a representative of Group 16, tellurene is a 2D elementary material and considered as a promising candidate for various applications in field-effect transistors,[32] photodetectors,[33] chemical sensor,[34] and solar cells.[35] Recent works have revealed the thickness-dependent band gap from 0.33 eV (bulk) to 0.92 eV (monolayer),[36-38] which enables its potential application in photocatalysis as cocatalyst. Moreover, it is noted that tellurene is resistive to oxygen molecules with air-stable performance at room temperature.[32] Based on these considerations, it is

expected to employ tellurene as a metal-free cocatalyst to achieve highly efficient photocatalytic H_2 production.

In this work, we perform theoretical investigations on the band structure of tellurene by density functional theory (DFT) calculations and verify the possibility of tellurene as a reduction cocatalyst. We synthesize tellurene (Te) nanosheets as a metal-free cocatalyst and investigate their thickness-dependent activity by combining with cadmium sulfide (CdS) photocatalyst. By depositing 1.0% Te nanosheets with thickness of 2-5 nm on the surface of CdS (Te/CdS), the resulting catalytic system exhibits an optimal photocatalytic hydrogen production rate of 234.4 μmol h^{-1} that exhibits 7.8 times improvement in comparison with bare CdS (30.2 μmol h^{-1}). The improved hydrogen evolution activity is attributed to the strong chemical correlation between CdS and Te, and electron-extracting capacity of Te cocatalyst, which is evidenced by ultrafast transient absorption (TA) spectra.

2. Experimental section

2.1 Preparation of tellurene nanosheets

Typically, 100 mg bulk Te powders were added into 100 mL isopropanol (IPA). Then, the Te/IPA slurry was subjected to a bath sonication to generate tellurene nanosheets with different thickness. The power, time, and temperature of bath sonication are 500 W, 24 h, and 5 ^{o}C, respectively. The suspension was first centrifuged at 500 rpm (28 xg) for 10 min to remove non-exfoliation bulk Te and the

suspension was reserved for further treatment. To obtain tellurene nanosheets with different thicknesses (30-50 nm, 10-20 nm, and 2-5 nm), the centrifugation strategy was employed. The detailed centrifugation strategy is shown in Supplementary data.

2.2 Preparation of Te/CdS

The CdS microspheres are prepared by one-step hydrothermal method (See the detailed procedures in Supplementary data). Te/CdS composites were fabricated by a one-step method. Typically, 100 mg CdS nanoparticles were dispersed into 100 mL IPA solution under bath sonication. After sonication for 30 min, 1 mL of Te dispersion was added into the above suspension. After 2 h sonication treatment (the temperature should be lower than 5 ºC), the mixture was further stirred for 12 h. The samples were collected by high-speed centrifugation, wash with ethanol, and freeze-dried. Through adjusting the addition volume of Te dispersion, Te/CdS with different Te loading amount (0.5 wt.%, 2 wt.%, 5 wt.%, 10 wt.%) were prepared. The synthetic methods of MoS_2/CdS and Pt/CdS are shown in Supplementary data.

2.3. Characterization Methods

X-ray diffraction (XRD) patterns of all samples were collected in the range 5-80° (2θ) using a RigakuD/MAX ⅢA diffract meter (Cu K radiation, λ =1.5418 Å), operated at 40 kV and 100 mA. The morphologies were characterized by transmission electron microscopy (TEM, JEM2011) and field emission scanning electron

microscopy (FESEM, JEOL 6700). The composition of all the samples was characterized by energy dispersive X-ray (EDX) attached to the high resolution transmission electron microscopy (HRTEM). High angle annular dark field scanning transmission electron microscopy (HAADF-STEM) image and elemental mapping were collected using a TEM (JEOL, JEM-2100F) equipped with EDX spectroscopy. The instrument employed for XPS studies was a Perkin-Elmer PHI 5000C ESCA system with Al Kα radiation operated at 250 W. The shift of the binding energy due to relative surface charging was corrected using the C1s level at 284.4 eV as an internal standard. Photo/electrochemical measurements were performed on a standard three electrode cell with a working electrode, a Pt wire as the counter electrode, and a saturated calomel electrode as the reference electrode in dark on an electrochemical workstation (Zahner, Zennium). The working electrode was prepared through a clean fluoride-tin oxide (FTO) deposited with a sample film. The aqueous solution of 0.5 M Na_2SO_4 purged with nitrogen gas was used as the electrolyte. Linear sweep voltammetry (LSV) curves were recorded in a lactic acid solution at a scan rate of 5 mV s^{-1} to obtain the polarization curves. Inductively coupled plasma-massspectrometry (ICP-MS, Agilent 7700x, USA) was employed to determine the compositions of the samples. The test details of Femtosecond-resolved transient absorption (TA) measurements are shown in Supplementary data.

2.4. Pt selective deposition

100 mg 1 wt.% Te/CdS was added into 100 mL aqueous solution containing 5% lactic acid, and then a certain amount of H_2PtCl_6 solution was added into the above suspension under ultrasound. The suspension was irradiated under a 300 W Xe lamp equipped with a UV-cutoff filter ($\lambda \geqslant 420$ nm). After 15 min photoreduction, the sample was collected by centrifuging, washed with ethanol and DI water three times.

2.5. Photocatalytic measurements

The photocatalytic hydrogen evolution experiments were conducted on an online photocatalytic hydrogen evolution system at ambient temperature (5 ^{o}C) under a 300 W Xe lamp irradiation equipped with an AM 1.5 solar simulator. 20 mg of catalyst was dispersed 100 mL of aqueous solution containing 5 mL lactic acid as sacrificial reagents under ultrasonic treatment, and subsequently the suspension was vacuumized for 1 h. Hydrogen evolution was analyzed by an online gas chromatograph (TCD, nitrogen as a carrier gas and 5 Å molecular sieve column). Once the photocatalytic reaction of a cycle test of 150 min was completed, the reactor was replenished with 3 mL lactic acid and degassed in vacuum before starting the subsequent cycle. The determination of the quantum efficiency (QE) for hydrogen evolution was performed by using a 300 W Xe lamp equipped with $\lambda \pm 20$ nm band-pass filter. The average intensity of irradiation was determined by a light intensity meter and the irradiation area was 37.9 cm^2. The number of incident photons (N) was calculated by equation (1). The quantum efficiency is calculated from equation (2).

$$N = \frac{E\lambda}{hc} \quad (1)$$

$$QE = \frac{2 * \text{the number of the evolved H2 molecules}}{\text{The number of incident photons}} \quad (2)$$

2.6. Computational details

The spin-polarized first-principles calculations based on the Density Functional Theory (DFT) were performed using the Vienna *Ab initio* Simulation Package (VASP)[39-41] to investigate the hydrogen evolution reaction (HER) performance on the CdS (0001) surface, free-standing and CdS-supporting 1T-MoS_2-like Te monolayer.[42] The Perdew-Burke-Ernzerhof (PBE) exchange-correlation functional[43] within the generalized gradient approximation (GGA) was employed to describe the exchange-correlation energy. The projector-augmented-wave (PAW)[44] method was adopted for the pseudopotentials. The energy cutoff for the plane wave basis expansion was set to 450 eV. The models were constructed with 2×2 supercells and the 15 Å vacuum layer added in the z directions to avoid the interactions between the atom layers and their mirror images. The atom positions were fully optimized with the force on each atom of 0.02 eV/Å for convergence criterion. The sampling in the Brillouin zone was set with 3×3×1 by the Monkhorst-Pack method.[45] The Gibbs free energy was calculated by $\triangle G_H = E_{tot} - E_{sub} - 1/2E_{H2} + 0.24$, where E_{tot}, E_{sub} and E_{H2} are the energy of the hydrogen adsorbed configuration, the energy of the catalyst and the energy of H_2 molecule, 0.24 eV represents the term of $\triangle E_{ZPE} - T\triangle S$[10], respectively. Three nonequivalent positions above the free-stranding and CdS-supporting Te monolayer, as well as the sites above the outmost S atom at the

top side and below the lowest Cd atom at the bottom side of the bare CdS (0001) surface were considered for hydrogen adsorption.

3. Results and discussion

3.1. Theoretical and experimental investigations of the possibility of Te as a cocatalyst

To explore the possibility of Te as a cocatalyst, we first conducted theoretical investigations based on DFT calculations. Figure S1 shows the constructed crystal structures of bulk Te, quad-, tri-, bi- and mono-layer Te. With reduced thickness from bulk to quad-, tri-, bi- and mono-layer, the corresponding band gaps substantially increase from 0.182 to 0.622, 0.789, 1.040, and 1.280 eV (Figure S2), respectively. With the reduction of the layer number of Te, the bandgap increases due to the quantum confinement effect, which offers opportunities to form favorable band alignment with photocatalysts. Besides, the reduced thickness endows Te nanosheets with large surface area and more exposed active sites, which contributes to strong chemical coupling with semiconductor photocatalysts. Moreover, compared with its bulk counterparts, 2D Te shows the upward shift of conduction band (CB) position (Figure S2), thereby giving rise to the improved reduction potential of photogenerated electrons injected from semiconductor photocatalysts.

To further verify the thickness-dependent properties experimentally, we synthesized three Te nanosheets with different thicknesses of 2-5 nm (Figure 1a-1e), 10-20 nm (Figure S3), and 30-50 nm (Figure S4) by a one-step liquid exfoliation followed by

high-speed centrifugation, which is confirmed by transmission electron microscopy (TEM), atomic force microscope (AFM), and X-ray diffraction (XRD) patterns. It should be noted that two extra XRD peaks at 2θ of 26° and 30° are indexed to TeO_2, indicating a small portion of Te is oxidized into TeO_2, which accords with the previous reports.[33] From ultraviolet visible diffuse reflectance spectra ((UV-Vis-DRS) and valence-band-XPS (VB-XPS) spectra (Figure S5), it can be observed that both of the band gap and CB energy increase with the decreased thickness (Table S1), in good agreement with the DFT calculation results.

3.2. Catalysts morphology and chemical environment characterizations

By combining experimental and theoretical investigations, we verify that Te can be expected as high-performance cocatalyst combined with photocatalysts. To investigate thickness-dependent cocatalytic activity, Te nanosheets with different thicknesses were used as cocatalysts to couple with CdS microsphere photocatalysts (Figure S6) through a facile one-step deposition. As the thickness of Te nanosheets decreases, a rapid enhancement in photocatalytic hydrogen evolution rates was observed (Figure 1f), unveiling the thickness-dependent cocatalytic activity of Te for hydrogen evolution. Owing to the highest cocatalytic activity of Te nanosheets with the thickness of 2-5 nm, the investigations on structure-activity correlations of Te/CdS are highly essential. The morphology and chemical composition of Te/CdS with 1 wt.% Te loading were firstly studied by TEM observations. As shown in Figure 2a,b, Te

nanosheets were attached on the surface of CdS microsphere to form a hybrid Te/CdS structure. More close TEM observation (Figure S7) shows the Te nanosheets keep ultrathin structure after compositing with CdS. Moreover, no obvious agglomeration for Te nanosheets can be seen after increasing or decreasing of Te depositing amount on CdS (Figure S8). The high resolution TEM (HRTEM) image (Figure 2c) shows an obvious boundary between CdS and Te, and two sets of lattice fringe spacings of 0.316 and 0.221 nm, corresponding to the (101) plane of CdS and (110) plane of Te, respectively. The element mapping image (Figure 2d) and the corresponding energy dispersive X-ray (EDX) spectrum (Figure 2e) of Te/CdS demonstrate that the three Cd, S, and Te elements are uniformly distributed, further confirming the successful decoration of Te nanosheets on CdS. XRD pattern (Figure 2f) of as-prepared Te/CdS sample shows characteristic peaks of CdS with hexagonal Wurtzite crystal structure, and no typical Te peaks can be observed owing to the low loading amount. The loading amount of Te (1.05 wt%) is quantified by inductively coupled plasma mass spectrometry (ICP-MS) methods (Table S2), which is close to the nominal mass ratio (1%) of Te to CdS.

To investigate whether the electronic coupling interface is formed between Te and CdS, which is the necessary prerequisite for interfacial charge transfer, we first construct a well-defined Te/CdS (0001) interface by DFT simulations (Figure 3a,b). The calculated lattice constant of 2D monolayer Te is 4.18 Å, close to the lateral constant of 4.13 Å for CdS. The negligible lattice mismatch is beneficial for

constructing the stable Te/CdS (0001) interface. The optimized interfacial distance is 2.96 Å, which is comparable with the length of 2.66 Å for the Cd-S bond in the vertical direction, yielding the adhesive energy of 0.49 J/m^2. The strong electron coupling effect is visualized at the interface (Figure 3c), where electron depletion mainly occurs to the outmost Cd atoms and the region between the first and second Te atom-layer, while accumulate at the interfacial region and exist as doughnut-like isosurfaces. Bader charge analysis indicates that the outmost Cd atom loses 0.77 electrons, of which 0.26 electrons transfer to Te and the rest electrons are grabbed by the coordinated S atoms. Besides, the calculated band structures (Figure 3d, Figure S2) indicate that the CB position of CdS is higher than that of Te, suggesting that the photogenerated electrons transfer from CdS to Te is thermodynamically feasible.

We further use X-ray photoelectron spectroscopy (XPS) to investigate the interfacial interactions between Te and CdS. The Te 3d XPS spectra (Figure 3e) for Te exhibit two peaks at the binding energies of 573.1 and 583.4 eV, assigning to $3d_{5/2}$ and $3d_{3/2}$ of element Te^0, respectively. The other evident doublet peaks at 576.1 and 586.5 eV correspond to Te^{4+} 3d peaks, suggesting the presence of TeO_2, which is in a good agreement with the XRD patterns. Compared with Te, the Te^0 3d peaks for Te/CdS shift to lower binding energy by ca. 0.3 eV, manifesting that an intimate contact between Te and CdS is formed at the interface. Furthermore, this decrease of binding energy of Te 3d in Te/CdS means an increase of electron concentration, revealing an electron transfer from CdS to Te.[46, 47] Besides, the Cd 3d (Figure 3f) and S 2p

(Figure 3g) peaks in Te/CdS are observed to shift to higher binding energies by ca. 0.3 eV as compared to those of bare CdS. To further uncover the electron transfer pathway, UV-DRS and VB-XPS spectra are measured. As displayed in Figure 3h, both pristine CdS and Te nanosheets show a visible light absorption with band gap energies (E_g) of 2.33 (Figure S9) and 1.80 eV (Figure S5b$_1$), respectively. Besides, according to the VB-XPS results (Figure 3i, Figure S5c$_1$), the VB energies (E_v) of CdS and Te are determined to be 1.34 and 1.45 eV, respectively. Therefore, the CB energies of CdS and Te are estimated at 0.99 and 0.35 eV from E_g - E_v, respectively, and the energy band configurations of CdS and Te can be illustrated in Figure 3j. The higher E_v value of CdS arouses the photo-generated electron transfer from CdS to Te, which is in a good agreement with the DFT simulation results. Besides, it is noted that the loading of Te nanosheets do not give rise to the shift of absorption edge (559 nm), suggesting Te is hybridized with CdS rather than doped into CdS. To better understand the electron transfer mechanism in Te/CdS, the reduction of Pt^{4+} in the lactic acid solution was carried out. As shown in Figure S10a, TEM observation demonstrates that Pt nanoparticles are selectively deposited on the surface of Te nanosheets. Furthermore, two sets of lattice fringe spacings of 0.221 and 0.196 nm (Figure S10b), corresponding to the (110) plane of Te and (200) plane of Pt, respectively, can be clearly observed. The EDX line scan (Figure S10c) further confirms that the Pt nanoparticles are deposited on the Te nanosheets rather than CdS microspheres, suggesting that Te can effectively capture photo-induced electron from

CdS and be regarded as active sites for H_2 evolution. Based on the above theoretical and experimental results, we can confirm both the strongly interfacial electronic coupling effect and electron flow direction from CdS to Te (Figure 3j), which is thermodynamically beneficial to improving charge separation efficiency of CdS.

3.3. Charge transfer behavior characterizations

The separation and migration efficiency of electron-hole pairs were further investigated by steady-state photoluminescence (PL) spectra (Figure 4a). The PL spectra show the remarkably quenched characteristic peak of CdS after depositing Te nanosheets as cocatalysts, indicating the longer lifetime of photo-induced electron exicited from CdS. To gain the intrinsic reason towards the PL spectra result, time-resolved PL decay spectra were measured and fitted by bi-exponential function. As observed in Figure 4b, in comparison to CdS, Te/CdS exhibits increased short (τ_1), long (τ_2), and average PL lifetimes, suggesting the introduction of Te onto CdS can suppress the recombination of photo-generated charge carriers. To further illustrate the improved charge separation efficiency in Te/CdS, linear sweep voltammetry (LSV) measurements were performed under visible light irradiation (Figure 4c). The LSV curves indicate that the Te/CdS has the higher cathodic current density for reducing H_2O to H_2 as compared to CdS. This enhanced catalytic capability was further corroborated by the transient photocurrent response and electrochemical impedance spectra (EIS). As shown in Figure 4d, Te/CdS displays a higher photocurrent response

relative to the pristine CdS, which implies the improved charge separation efficiency in the bulk of Te/CdS. On the other hand, a much smaller semicircle diameter in the EIS for Te/CdS is observed (Figure 4e), suggesting the apparently enhanced interfacial charge carriers transfer on the surface of Te/CdS.

Moreover, ultrafast transient absorption (TA) spectra were collected to analyze the electron dynamics. 400 nm laser and white light continuum of 440-700 nm are selected as pump pulse and probe pulse, respectively. Upon pump pulse excitation, both CdS (Figure 4f) and Te/CdS (Figure 4g) show the distinctly negative absorption peak at 525 nm, which is ascribed to photo-bleaching of the ground state (GS) absorption.[48] TA kinetic decay traces of these two samples are featured by initial signal build-ups within 10 ps and subsequent recovery processes with different durations (Figure 4h). The recovery time of Te/CdS (＜200 ps) is much shorter than that of CdS (＞800 ps), suggesting the photogenerated electrons can rapidly transfer from CdS to Te.[49, 50]

3.4. Photocatalytic hydrogen evolution performance

As expected, the coupling of Te nanosheets with CdS indeed contributes to an obvious improvement in the photocatalytic performance with the presence of lactic acid as an electron donor (Figure 5a). The isotopic tracer experiments were carried out to reveal that the generated hydrogen comes from water rather than lactic acid (Figure S11). With the optimal loading of 1 wt.% Te, Te/CdS shows the highest photocatalytic

H_2 production rate of 234.4 μmol h^{-1}, which is 7.8 times higher than that of bare CdS (30.2 μmol h^{-1}). Moreover, Te alone exhibits negligible H_2 production rate owing to its poor ability of formation of photoexcited electrons and holes, further ascertaining the cocatalyst role of Te. TEM and AFM images (Figure S12) of the recovered bare Te after photocatalysis demonstrate that the morphology and thickness remain the same with the initial Te nanosheets, indicating its structure stability. To highlight the advantage of this metal-free Te cocatalyst, MoS_2/CdS (Figure S13) and Pt/CdS (Figure S14) with the same loading cocatalyst amount (Table S2) are prepared (It is noted that MoS_2 and Pt are two state-of-the-art candidates in noble-metal-free and noble-metal cocatalysts, respectively). As shown in Figure 5a, Te/CdS demonstrates higher performance as compared to MoS_2/CdS and Pt/CdS. Besides, the wavelength dependent apparent quantum efficiency (AQE) of photocatalytic H_2 evolution is illustrated in Figure 5b, in which a high AQE of 11.4% and 5.6% can be obtained at the fixed wavelength of 420 nm and 475 nm, respectively, which is comparable to most of CdS merged with the previously reported metal-free and noble-metal-free cocatalysts (Table S3). When the light absorption at wavelengths is longer than 550 nm, the AQE value is close to zero due to the low absorption efficiency for CdS in the visible-light region beyond 550 nm. Moreover, the durability of Te/CdS with the optimal Te loading is further evaluated. As displayed in Figure 5c, Te/CdS maintained stable photocatalytic H_2 evolution rate after 5 cycles accumulated 10 h. TEM observations (Figure S15) show that the Te nanosheets maintain ultrathin structure,

indicating the structure stability of Te as cocatalysts. XRD patterns (Figure S16a) and XPS spectra (Figure S16b-d) of Te/CdS before and after the photocatalytic reaction show negligible change. The concentrations of Cd, S, and Te elements in Te/CdS after the photocatalytic reaction are almost the same as their initial concentrations by the ICP-MS analysis (Table S4). Furthermore, the Gibbs free energy of the intermediate state, ΔG_H, is calculated as an indicator to evaluate hydrogen evolution reaction activity. As shown in Figure 5d and Figure S17, the calculation results show that Te/CdS has the relatively moderate ΔG_H of 0.56 eV as compared to bare CdS and Te, indicating the lower energy barrier for hydrogen evolution of Te/CdS, which coincides with the experimental results. Consequently, the electron transfer route in the Te/CdS hybrids can be illustrated in Figure 5e. Under solar light irradiation, electrons are excited from VB to CB of CdS, which then transfers to Te rapidly, thus achieving efficient electron-hole separation in Te/CdS system. Subsequently, owing to the excellent charge mobility of Te, the electrons captured by Te can migrate to active sites on Te to involve in the hydrogen production reaction.

4. Conclusion

In summary, we design tellurene nanosheets as a highly efficient cocatalyst and investigated the effect of thickness of tellurene on photocatalytic performance for hydrogen production. Few-layer tellurene nanosheets with thickness of 2-5 nm are rationally integrated with CdS to induce a high photocatalytic hydrogen evolution rate

(234.4 μmol h^{-1}) and an apparent quantum efficiency of 11.4% at 420 nm. The DFT calculations and time-resolved spectroscopy suggest that the high photocatalytic performance is ascribed to the highly efficient charge separation and migration from CdS to tellurene and the rapid H_2 evolution on tellurene nanosheets with massive active sites and high charge mobility. This study demonstrates high-performance and cheap metal-free cocatalytic materials for photocatalytic water splitting and other energy conversion systems.

Acknowledgment

This work was supported by the Research Grant Council of Hong Kong (N_PolyU540/17), the Hong Kong Polytechnic University (Grants G-YBPS and Grants G-YW2A), and the Science, Technology and Innovation Commission of Shenzhen (JCYJ20180507183424383).

AUTHOR INFORMATION

Corresponding Author

*Email: ychai@polyu.edu.hk

Author contributions

Y.C. supervised the project. B.Q. and Y.C. conceived the idea, designed all experiments, and wrote the manuscript. B.Q. J.W. and Z.L. performed synthesis and characterizations of catalysts. B.Q. N.Z. and L.C. carried out photo/eletrocatalytic measurement and discussed the results. C.W. performed the DFT simulations. X.T.

revised the manuscript and provided helpful suggestions. All authors provided constructive comments on the manuscript.

Appendix A. Supplementary data

Supplementary data associated with this article can be found, in the online version, at http://dx.doi.org/10.1016/j.apcatb. xxxx.xx.xxx

Notes

The authors declare no competing financial interest.

References

[1] Z. Wang, C. Li, K. Domen, Recent developments in heterogeneous photocatalysts for solar-driven overall water splitting, Chem. Soc. Rev., 48 (2019) 2109-2125.

[2] B. Qiu, M. Xing, J. Zhang, Recent advances in three-dimensional graphene based materials for catalysis applications, Chem. Soc. Rev., 47 (2018) 2165-2216.

[3] X. Zhang, H. Liu, Y. Shi, J. Han, Z. Yang, Y. Zhang, C. Long, J. Guo, Y. Zhu, X. Qiu, Boosting CO_2 conversion with terminal alkynes by molecular architecture of graphene oxide-supported Ag nanoparticles, Matter, 3 (2020) 558-570.

[4] Z. Yang, X. Zhang, C. Long, S. Yan, Y. Shi, J. Han, J. Zhang, P. An, L. Chang, Z. Tang, Covalently anchoring cobalt phthalocyanine on zeolitic imidazolate frameworks for efficient carbon dioxide electroreduction, CrystEngComm, 22 (2020) 1619-1624.

[5] J. Ran, J. Zhang, J. Yu, M. Jaroniec, S.Z. Qiao, Earth-abundant cocatalysts for semiconductor-based photocatalytic water splitting, Chem. Soc. Rev., 43 (2014) 7787-7812.

[6] T. Takata, J. Jiang, Y. Sakata, M. Nakabayashi, N. Shibata, V. Nandal, K. Seki, T. Hisatomi, K. Domen, Photocatalytic water splitting with a quantum efficiency of almost unity, Nature, 581 (2020) 411-414.

[7] A. Naldoni, M. Altomare, G. Zoppellaro, N. Liu, S.t.p.n. Kment, R. Zbořil, P. Schmuki, Photocatalysis with reduced TiO_2: from black TiO_2 to cocatalyst-free hydrogen production, ACS Catal., 9 (2018) 345-364.

[8] S. Cao, C.J. Wang, W.F. Fu, Y. Chen, Metal Phosphides as Co-Catalysts for Photocatalytic and Photoelectrocatalytic Water Splitting, ChemSusChem, 10 (2017) 4306-4323.

[9] Z. Sun, H. Zheng, J. Li, P. Du, Extraordinarily efficient photocatalytic hydrogen evolution in water using semiconductor nanorods integrated with crystalline Ni_2P cocatalysts, Energ. Environ. Sci., 8 (2015) 2668-2676.

[10] B. Qiu, L. Cai, N. Zhang, X. Tao, Y. Chai, A Ternary Dumbbell Structure with Spatially Separated Catalytic Sites for Photocatalytic Overall Water Splitting, Adv. Sci., 7 (2020) 1903568.

[11] W. Bi, L. Zhang, Z. Sun, X. Li, T. Jin, X. Wu, Q. Zhang, Y. Luo, C. Wu, Y. Xie, Insight into electrocatalysts as co-catalysts in efficient photocatalytic hydrogen evolution, ACS Catal., 6 (2016) 4253-4257.

[12] M. Xing, B. Qiu, M. Du, Q. Zhu, L. Wang, J. Zhang, Spatially separated CdS shells exposed with reduction surfaces for enhancing photocatalytic hydrogen evolution, Adv. Funct. Mater., 27 (2017) 1702624.

[13] B. Qiu, Y. Deng, Q. Li, B. Shen, M. Xing, J. Zhang, Rational design of a unique ternary structure for highly photocatalytic nitrobenzene reduction, J. Phys. Chem. C, 120 (2016) 12125-12131.

[14] Q. Zhu, Z. Xu, Q. Yi, M. Nasir, M. Xing, B. Qiu, J. Zhang, Prolonged electron lifetime in sulfur vacancy-rich ZnCdS nanocages by interstitial phosphorus doping for photocatalytic water reduction, Mater. Chem. Front., 4 (2020) 3234-3239.

[15] C. Long, K. Wang, Y. Shi, Z. Yang, X. Zhang, Y. Zhang, J. Han, Y. Bao, L. Chang, S. Liu, Tuning the electronic structure of PtRu bimetallic nanoparticles for promoting the hydrogen oxidation reaction in alkaline media, Inorg. Chem. Front., 6 (2019) 2900-2905.

[16] J. Yang, D. Wang, H. Han, C. Li, Roles of cocatalysts in photocatalysis and photoelectrocatalysis, Acc. Chem. Res., 46 (2013) 1900-1909.

[17] S. Zhang, X. Liu, C. Liu, S. Luo, L. Wang, T. Cai, Y. Zeng, J. Yuan, W. Dong, Y. Pei, MoS_2 quantum dot growth induced by S vacancies in a $ZnIn_2S_4$ monolayer: atomic-level heterostructure for photocatalytic hydrogen production, ACS Nano, 12 (2018) 751-758.

[18] M. Zhu, Z. Sun, M. Fujitsuka, T. Majima, Z-Scheme Photocatalytic Water Splitting on a 2D Heterostructure of Black Phosphorus/Bismuth Vanadate Using Visible Light, Angew. Chem. Int. Ed., 57 (2018) 2160-2164.

[19] X. Chang, T. Wang, P. Yang, G. Zhang, J. Gong, The development of cocatalysts for photoelectrochemical CO_2 reduction, Adv. Mater., 31 (2019) 1804710.

[20] B. Qiu, M. Xing, J. Zhang, Mesoporous TiO_2 nanocrystals grown in situ on graphene aerogels for high photocatalysis and lithium-ion batteries, J. Am. Chem. Soc., 136 (2014) 5852-5855.

[21] C. Ding, J. Shi, Z. Wang, C. Li, Photoelectrocatalytic water splitting: significance of cocatalysts, electrolyte, and interfaces, ACS Catal., 7 (2017) 675-688.

[22] G. Zuo, Y. Wang, W.L. Teo, A. Xie, Y. Guo, Y. Dai, W. Zhou, D. Jana, Q. Xian, W. Dong, Y. Zhao, Ultrathin $ZnIn_2S_4$ Nanosheets Anchored on $Ti_3C_2T_X$ MXene for Photocatalytic H_2 Evolution, Angew. Chem. Int. Ed., 59 (2020) 11287-11292.

[23] F. Xu, K. Meng, B. Zhu, H. Liu, J. Xu, J. Yu, Graphdiyne: a new photocatalytic CO_2 reduction cocatalyst, Adv. Funct. Mater., 29 (2019) 1904256.

[24] M. Wang, L. Cai, Y. Wang, F. Zhou, K. Xu, X. Tao, Y. Chai, Graphene-draped semiconductors for enhanced photocorrosion resistance and photocatalytic properties, J. Am. Chem. Soc., 139 (2017) 4144-4151.

[25] K. Chang, Z. Mei, T. Wang, Q. Kang, S. Ouyang, J. Ye, MoS_2/graphene cocatalyst for efficient photocatalytic H_2 evolution under visible light irradiation, ACS Nano, 8 (2014) 7078-7087.

[26] K. Zhang, B. Jin, C. Park, Y. Cho, X. Song, X. Shi, S. Zhang, W. Kim, H. Zeng, J.H. Park, Black phosphorene as a hole extraction layer boosting solar water splitting of oxygen evolution catalysts, Nat. Commun., 10 (2019) 1-10.

[27] M. Zhu, S. Kim, L. Mao, M. Fujitsuka, J. Zhang, X. Wang, T. Majima, Metal-free photocatalyst for H_2 evolution in visible to near-infrared region: black phosphorus/graphitic carbon nitride, J. Am. Chem. Soc., 139 (2017) 13234-13242.

[28] J. Di, X. Zhao, C. Lian, M. Ji, J. Xia, J. Xiong, W. Zhou, X. Cao, Y. She, H. Liu, Atomically-thin Bi_2MoO_6 nanosheets with vacancy pairs for improved photocatalytic CO_2 reduction, Nano Energy, 61 (2019) 54-59.

[29] J. Ran, B. Zhu, S.Z. Qiao, Phosphorene Co-catalyst Advancing Highly Efficient Visible-Light Photocatalytic Hydrogen Production, Angew. Chem. Int. Ed., 56 (2017) 10373-10377.

[30] A. Castellanos-Gomez, L. Vicarelli, E. Prada, J.O. Island, K. Narasimha-Acharya, S.I. Blanter, D.J. Groenendijk, M. Buscema, G.A. Steele, J. Alvarez, Isolation and characterization of few-layer black phosphorus, 2D Mater., 1 (2014) 025001.

[31] X. Zhu, T. Zhang, Z. Sun, H. Chen, J. Guan, X. Chen, H. Ji, P. Du, S. Yang, Black phosphorus revisited: a missing metal-free elemental photocatalyst for visible light hydrogen evolution, Adv. Mater., 29 (2017) 1605776.

[32] Y. Wang, G. Qiu, R. Wang, S. Huang, Q. Wang, Y. Liu, Y. Du, W.A. Goddard, M.J. Kim, X. Xu, Field-effect transistors made from solution-grown two-dimensional tellurene, Nat. Electron., 1 (2018) 228-236.

[33] Z. Xie, C. Xing, W. Huang, T. Fan, Z. Li, J. Zhao, Y. Xiang, Z. Guo, J. Li, Z. Yang, Ultrathin 2D nonlayered tellurium nanosheets: facile liquid-phase exfoliation, characterization, and photoresponse with high performance and enhanced stability, Adv. Funct. Mater., 28 (2018) 1705833.

[34] D. Wang, A. Yang, T. Lan, C. Fan, J. Pan, Z. Liu, J. Chu, H. Yuan, X. Wang, M. Rong, Tellurene based chemical sensor, J. Mater. Chem. A, 7 (2019) 26326-26333.

[35] K. Wu, H. Ma, Y. Gao, W. Hu, J. Yang, Highly-efficient heterojunction solar cells based on two-dimensional tellurene and transition metal dichalcogenides, J. Mater. Chem. A, 7 (2019) 7430-7436.

[36] J. Qiao, Y. Pan, F. Yang, C. Wang, Y. Chai, W. Ji, Few-layer Tellurium: one-dimensional-like layered elementary semiconductor with striking physical properties, Sci. Bull., 63 (2018) 159-168.

[37] J. Peng, Y. Pan, Z. Yu, J. Wu, J. Wu, Y. Zhou, Y. Guo, X. Wu, C. Wu, Y. Xie, Two‐Dimensional Tellurium Nanosheets Exhibiting an Anomalous Switchable Photoresponse with Thickness Dependence, Angew. Chem. Int. Ed., 57 (2018) 13533-13537.

[38] W. Wu, G. Qiu, Y. Wang, R. Wang, P. Ye, Tellurene: its physical properties, scalable nanomanufacturing, and device applications, Chem. Soc. Rev., 47 (2018) 7203-7212.

[39] G. Kresse, J. Furthmuller, Efficiency of ab-initio total energy calculations for metals and semiconductors using a plane-wave basis set, Comput. Mater. Sci., 6 (1996) 15-50.

[40] G. Kresse, J. Furthmuller, Efficient iterative schemes for ab initio total-energy calculations using a plane-wave basis set, Phy. Rev. B, 54 (1996) 11169-11186.

[41] G. Kresse, J. Hafner, Ab initio molecular-dynamics simulation of the liquid-metal–amorphous-semiconductor transition in germanium, Phys. Rev. B, 49 (1994) 14251-14269.

[42] Z. Zhu, X. Cai, S. Yi, J. Chen, Y. Dai, C. Niu, Z. Guo, M. Xie, F. Liu, J.-H. Cho, Y. Jia, Z. Zhang, Multivalency-Driven Formation of Te-Based Monolayer Materials: A Combined First-Principles and Experimental study, Phys. Rev. Lett., 119 (2017) 106101.

[43] J. Perdew, J.A. Chevary, S.H. Vosko, K. Jackson, M. Pederson, D.J. Singh, C. Fiolhais, Atoms, molecules, solids, and surfaces: Applications of the generalized gradient approximation for exchange and correlation, Phys. Rev. B, 46 (1992) 6671-6687.

[44] P.E. Blochl, Projector Augmented-Wave Method, Phys. Rev. B, 50 (1994) 17953-17979.

[45] H.J. Monkhorst, J.D. Pack, Special points for Brillouin-zone integrations, Phys. Rev. B, 13 (1976) 5188-5192.

[46] L. Zhuang, L. Ge, Y. Yang, M. Li, Y. Jia, X. Yao, Z. Zhu, Ultrathin iron-cobalt oxide nanosheets with abundant oxygen vacancies for the oxygen evolution reaction, Adv. Mater., 29 (2017) 1606793.

[47] Q. Zhu, B. Qiu, H. Duan, Y. Gong, Z. Qin, B. Shen, M. Xing, J. Zhang, Electron directed migration cooperated with thermodynamic regulation over bimetallic NiFeP/g-C_3N_4 for enhanced photocatalytic hydrogen evolution, Appl. Catal. B: Environ., 259 (2019) 118078.

[48] H. Zhang, P. Zhang, M. Qiu, J. Dong, Y. Zhang, X.W. Lou, Ultrasmall MoO_x clusters as a novel cocatalyst for photocatalytic hydrogen evolution, Adv. Mater., 31 (2019) 1804883.

[49] H.-Q. Xu, J. Hu, D. Wang, Z. Li, Q. Zhang, Y. Luo, S.-H. Yu, H.-L. Jiang, Visible-light photoreduction of CO_2 in a metal–organic framework: boosting

electron–hole separation via electron trap states, J. Am. Chem. Soc., 137 (2015) 13440-13443.

[50] X. Wu, H. Zhang, J. Dong, M. Qiu, J. Kong, Y. Zhang, Y. Li, G. Xu, J. Zhang, J. Ye, Surface step decoration of isolated atom as electron pumping: Atomic-level insights into visible-light hydrogen evolution, Nano Energy, 45 (2018) 109-117.

Figures

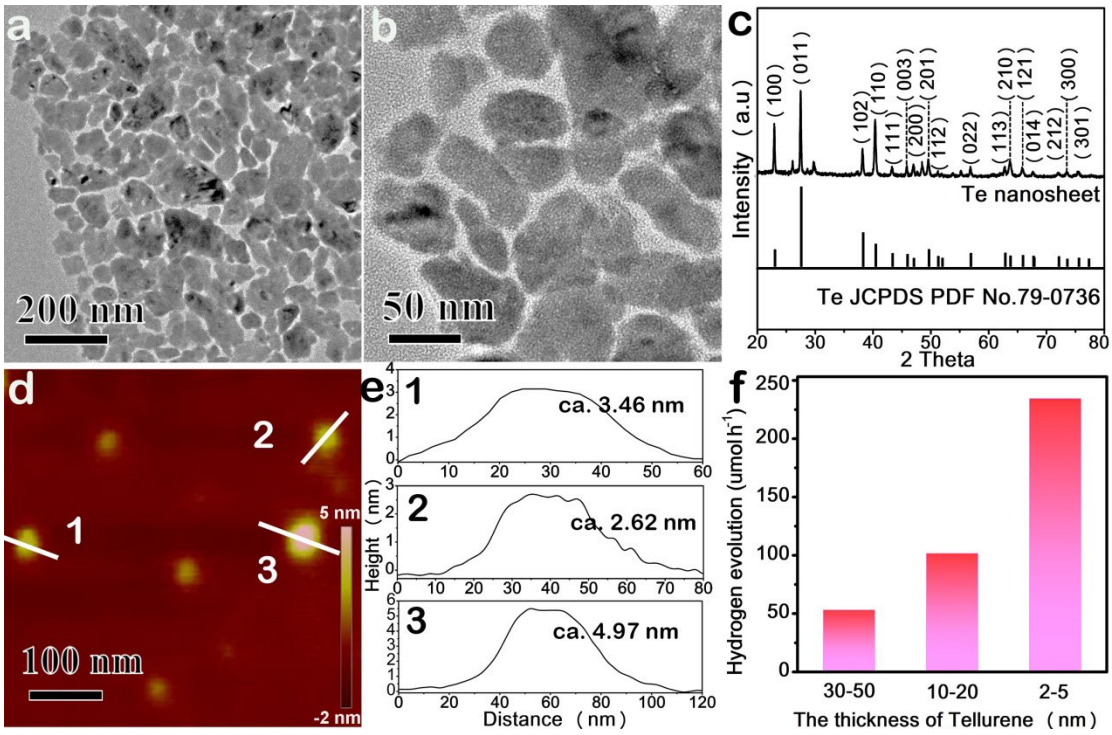

Figure 1. Characterization of ultrathin 2D Te nanosheets. (**a,b**) TEM images and (**c**) XRD pattern; (**d**) AFM image illustrating thickness; (**e**) the corresponding height profile; (**f**) A comparison of the photocatalytic hydrogen evolution rates of CdS coupled with 1.0 wt % Te nanosheets with different thicknesses (20 mg catalyst in 100 mL aqueous solution containing 5 mL lactic acid).

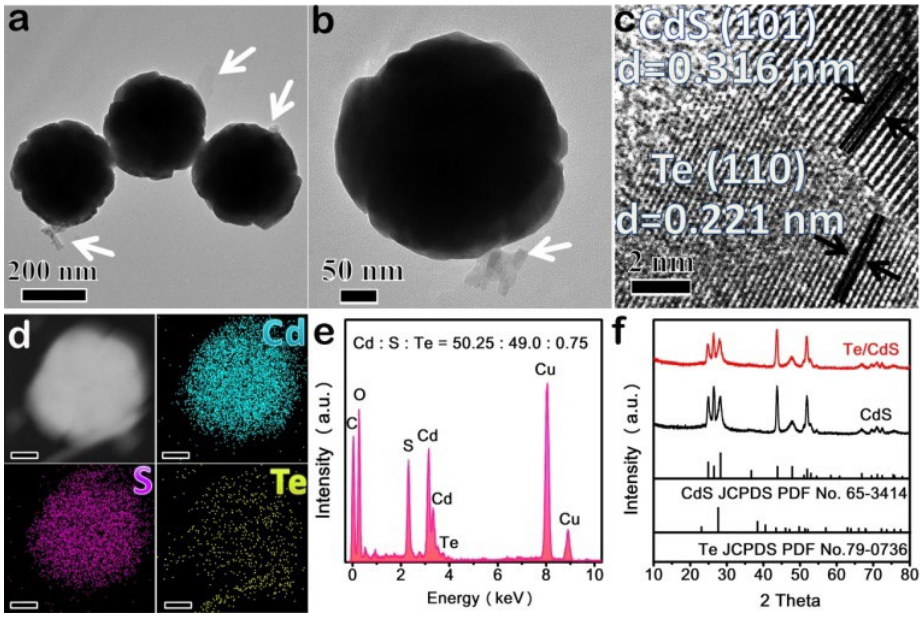

Figure 2. Components and elements distribution. (a,b) TEM, (c) HRTEM images, (d) the element mapping of Cd, S, and Te, and (e) the corresponding EDX spectrum of Te/CdS with 1 wt.% Te loading. (f) XRD patterns of Te/CdS with 1 wt.% Te loading and CdS.

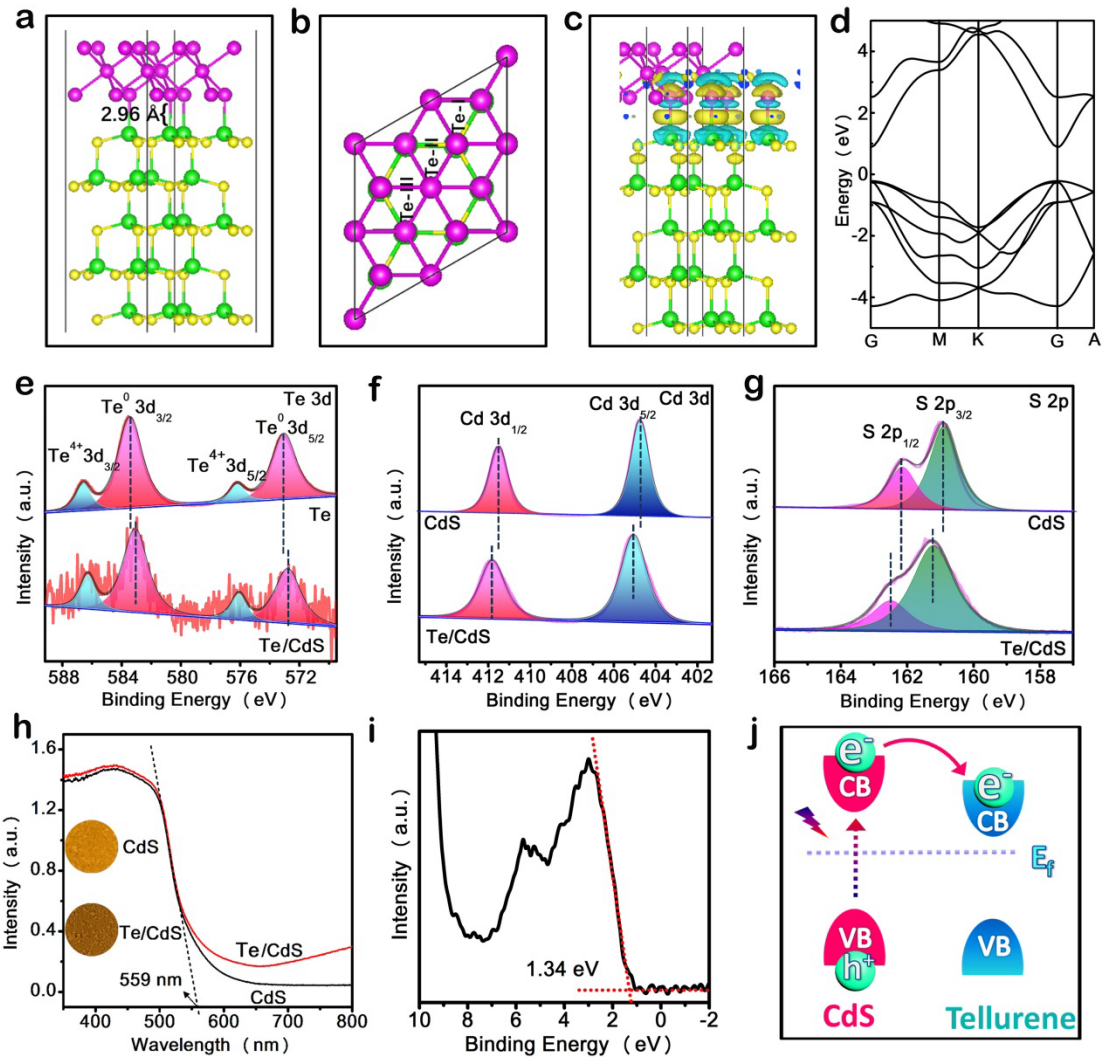

Figure 3. Theoretical simulations and experimental studies. (a) Side view and (b) top view of the optimized Te/CdS (0001) heterostructure. Te-I, Te-II, Te-III represent the first, second and third Te atom layer, respectively. (c) Charge density difference [$\triangle\rho$ = ρ(Te/CdS) − ρ(Te) − ρ(CdS)] of Te/CdS (0001) heterostructure. Electron excess and deficiency were displayed as yellow and light blue iso-surfaces, respectively, with the level of 0.003 e Å^{-3}. (d) The calculated band structure of CdS. (e) High-resolution Te 3d XPS spectra of Te and Te/CdS. High-resolution Cd 3d (f) and S 2p (g) XPS spectra of CdS and Te/CdS. (h) UV-Vis spectra of Te and Te/CdS. The insets show the colors

of CdS and Te/CdS. (i) VB-XPS spectrum of CdS. (j) Band alignments in CdS and Te/CdS. The Te loading amount of the above mentioned Te/CdS for experimental characterization is 1 wt.%.

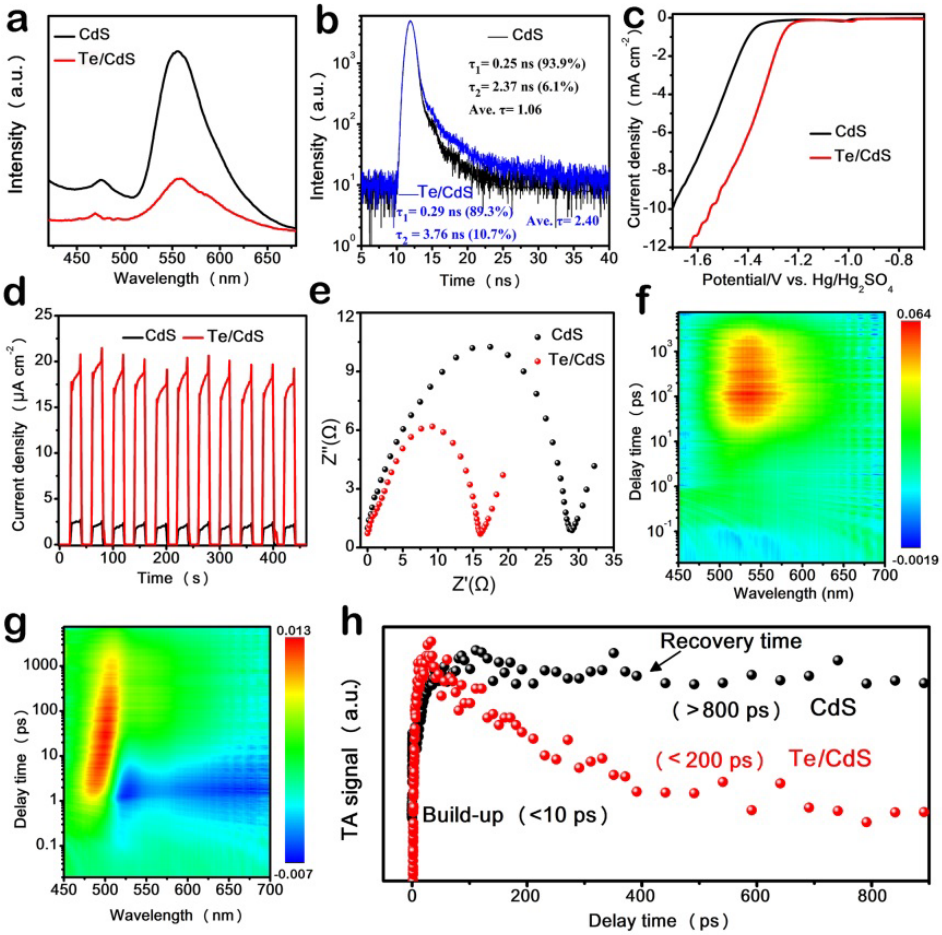

Figure 4. Photo/electrochemical properties. (a) PL spectra, (b) time-resolved PL decay spectra, (c) polarization curves, (d) transient photocurrents, and (e) EIS Nyquist plots of CdS and Te/CdS. 2D pseudo-color plot of TA spectra of CdS (f) and Te/CdS (g) at the excitation wavelength of 400 nm (x-axis, y-axis, and colors mean probe wavelength, pump probe delay, and change of absorbance, respectively.) (h) Ultrafast TA signals of CdS and Te/CdS. The Te loading amount of the above mentioned Te/CdS for experimental characterization is 1 wt.%.

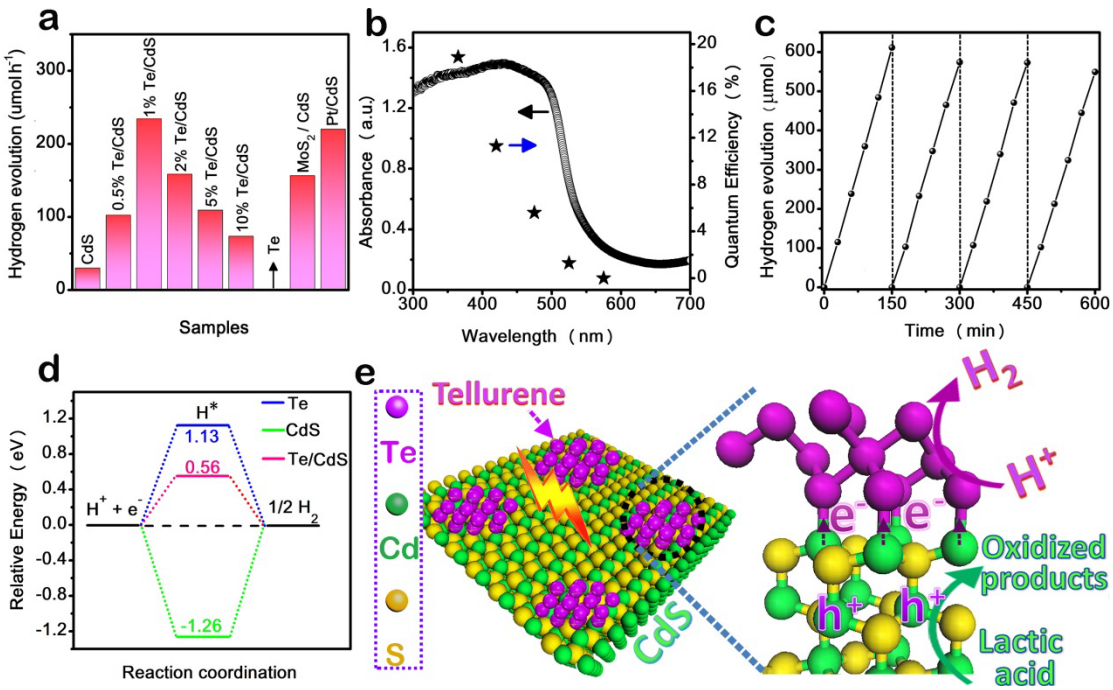

Figure 5. Photocatalytic performance, stability, and mechanism. (a) A comparison of the photocatalytic H_2 evolution activities of Te/CdS with different loading amount of Te, MoS_2/CdS and Pt/CdS (20 mg catalyst in 100 mL aqueous solution containing 5 mL lactic acid). (b) The wavelength dependent QE of H_2 evolution over 1.0 wt % Te/CdS. (c) Recycling H_2 evolution tests for Te/CdS with 1.0 wt % Te loading amount under Xe lamp irradiation equipped with AM 1.5. (d) Free energy diagram for hydrogen adsorption on CdS, Te, and Te/CdS. (e) The schematic illustration of the photocatalytic H_2 evolution mechanism on Te/CdS.